ELSEVIER

Effects of cell defects on the mechanical and thermal properties of carbon honeycombs

Yao Du , Jianli Zhou , Penghua Ying , Jin Zhang [*]

School of Science, Harbin Institute of Technology, Shenzhen 518055, China

ARTICLE INFO

ABSTRACT

Cell defects are inevitable during the fabrication of carbon honeycombs (CHCs), which, however, were tacitly ignored in previous studies. In this work, the effects of defects including Stone-Wales (SW) defect and single-wall vacancy (SV) defect on the mechanical and thermal properties of CHCs are investigated by using molecular dynamics simulations. Our results show that the Young's modulus of CHCs has nearly a constant value around 16.5 GPa, which is almost independent with the defect concentration. However, the tensile strength and fracture strain are reduced by about 40% and 20%, respectively, when the CHCs have a defect concentration of 2%. Additionally, the influence of SV defect on the fracture properties of CHCs is generally larger than that of its SW counterpart. The influence of cell defects on the mechanical properties of CHCs is well explained by the theories of damage and fracture mechanics. Our simulation results also show a reduction in the thermal conductivity of CHCs containing SW and SV defects. This reduction can be up to 23% when the defect concentration of CHCs is 2%. The reduced thermal conductivity observed in defective CHCs can be attributed to the wavy configuration of the component graphene nanoribbons in defective cells, which can increase the phonon scattering of CHCs. In addition, the reduced heat capacity of CHCs with SV defects can be another important factor inducing the reduction in their thermal conductivity.

1. Introduction

As the most basic element in nature, carbon can adopt various hybridizations including *sp*, *sp*² and *sp*³. In the past decades, numerous carbon allotropes have been successfully discovered and synthesized. For example, zero-dimensional fullerenes observed in 1985 [1] are found to have high electric conductivity, specific surface area and well-ordered structure [2]. These remarkable properties make them appealing in the energy conversion applications [2]. Iijima's report of carbon nanotubes (CNTs) in 1991 [3] has inspired growing research interest in these one-dimensional carbon materials. Superior mechanical and thermal properties such as ultrahigh Young's modulus (~1000 GPa) [4,5] and thermal conductivity (~6600 W/mK) [6] are observed in CNTs. These excellent material properties are now being exploited in diverse applications including nanosensors, nanotweezers and composite materials [7,8]. In 2004, two-dimensional (2D) graphene was successfully isolated through mechanical exfoliation [9]. As the first 2D material discovered in the world, graphene has attracted worldwide research interest due to its remarkable properties. Owing to its *sp*²

hybridization, graphene is known to be one of the strongest materials with the Young's modulus of 1TPa and tensile strength of 130 GPa [10]. Moreover, a high thermal conductivity around 4000 W/mK is also detected in the single-layer graphene (SLG) [11]. Owing to these extraordinary properties, graphene has a great potential in various engineering applications such as flexible electronics [12], photodetectors [13] and nanocomposites [14]. Although numerous remarkable properties have been observed in aforementioned low-dimensional carbon nanomaterials, the low-dimensional structure restricts their applications in wider aspects. Therefore, numerous researchers desire to build three-dimensional (3D) carbon nanomaterials based on the already synthesized low-dimensional nanostructures such as graphene and CNTs. However, some initial attempts indicate that the constructed 3D carbon nanomaterials usually cannot inherit the outstanding properties of their low-dimensional components. For example, a significant reduction in mechanical and thermal properties is generally observed in the 3D carbon derivatives constructed by staggering graphene sheets or vertical arraying CNTs [15–17]. A possible explanation for this performance reduction is that, the interaction between different blocks in constructed
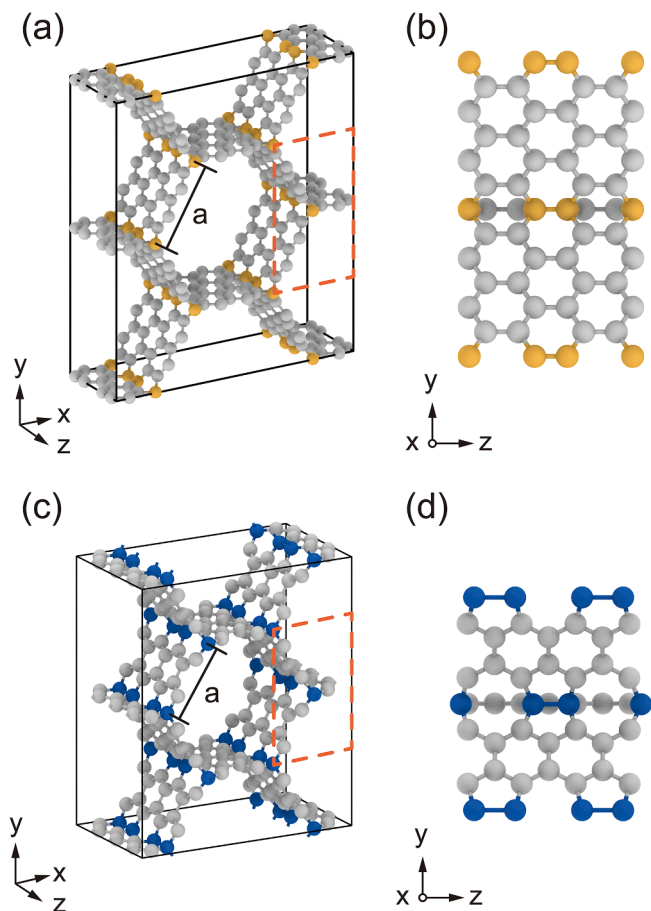

Fig. 1. The schematics of (a) the armchair CHC and (c) the zigzag CHC. The length of sidewall is *a*. (b) and (d) are side views of the atomic configuration of the two types of CHCs, which correspond the red dotted regions in (a) and (c), respectively. The yellow and blue balls represent atoms locating at the junctions in armchair and zigzag CHC, respectively. (For interpretation of the references to colour in this figure legend, the reader is referred to the web version of this article.)

3D carbon nanomaterials is dominated by weak van der Waals bonding rather than covalent bonding [18].

To overcome the performance reduction in the stacked 3D carbon nanomaterials, in the past decades, great efforts have been made to propose and fabricate new stable 3D carbon nanomaterials. Among them, the carbon honeycombs (CHCs) have attracted the most attention, because they have been successfully synthesized in experiments recently by the deposition of vacuum-sublimated graphite [19]. The experiment demonstrates that CHCs have high stability [19,20]. Meanwhile, due to their ultralarge surface-to-volume ratio [19], CHCs can be utilized for gas and liquid storage and also can be served as matrices for composites. Based on density functional theory (DFT) calculations and molecular dynamics (MD) simulations, numerous remarkable mechanical properties of CHCs such as high specific strength, strong anisotropic Poisson's effect, and high ductility have been reported in previous studies [21–29]. Meanwhile, some works also reveal that the thermal conductivity of CHCs is larger than most engineering materials, which is able to be tuned by changing the in-plane cell size length [22,23,30,31]. These superior properties make CHCs appealing for using in various engineering practices [19,20]. It is noted that most of the existing studies assume that CHCs possess a regular and defect-free hexagonal honeycomb [22–27,29,30]. However, during the fabrication of CHCs, cell defects are usually inevitable, which thus should be considered in the studies of CHCs. Although Zhang et al. [21] recently analyzed the compression behavior of CHCs with Stone-Wales (SW) defects, to our

best knowledge, the effect of cell defects on the mechanical and thermal properties of CHCs remains unexplored.

In this paper, the influence of cell defects on the mechanical and thermal properties of CHCs is investigated by using MD simulations. Both SW and vacancy defects are considered, since they are two common defects observed in carbon-based nanomaterials. Here, MD-based tensile tests are utilized to investigate the mechanical properties of CHCs, while non-equilibrium molecular dynamics (NEMD) simulations are performed to study their thermal properties. The dependence of the Young's modulus, tensile strength, fracture strain and thermal conductivity on the defect concentration of CHCs is comprehensively discussed. In addition, efforts are also made to reveal the mechanism behind the influence of cell defects on the mechanical and thermal properties of CHCs.

2. Methodology

2.1. Construction of defective CHCs

According to the previous report [21], the essential method to construct a CHC is through connecting three graphene nanoribbons (GNRs) along different edges to form a stable junction. There are two types of CHCs with different junctions. One is formed by the armchair edges of GNRs, which is, namely, the armchair CHC as shown in Fig. 1a and b. The other type is constructed by the zigzag edges of GNRs, which is, namely, the zigzag CHC as shown in Fig. 1c and d. Different to the carbon atoms in component graphene cell walls that have the sp^2 hybridization, a line of sp^3-bonded carbon atoms is found in the junctions of three GNRs. According to previous studies [21,23,27,32], the zigzag and armchair CHCs have the similar mechanical and thermal behaviors. Thus, to simplify our analysis without losing generality, in the present study only the armchair CHCs with cell defects were considered, since the major objective of this work is to study the effects of cell defects on the mechanical and thermal properties of CHCs.

The defect-free and defective CHCs considered in the current study are illustrated in Fig. 2. Specifically, the perspective views of defect-free and defective CHCs are shown in the left inset of Fig. 2a–c, while Fig. 2d and e illustrate the side and front views of defect-free CHCs, respectively. Here, the defect-free CHCs have a sidewall width *a* of 7.38 Å. As shown in the right inset of Fig. 2b, an SW defect can be created by rotating one sidewall by 90° in perfect CHCs. As a result, four hexagons change into two heptagons and two pentagons. Actually, similar heptagon and pentagon cell structures are widely observed in the CHCs synthesized in experiments [19,33], which indicates the possible existence of SW defects in real CHCs. The single-wall vacancy (SV) defect as shown in the right inset of Fig. 2c can be formed by removing one sidewall in perfect CHCs, which leads to the transformation of four hexagons into one octagon and two pentagons. It is worth mentioning that the SV defect in CHCs considered here is topologically similar to the bivacancy defect in graphene [34]. In this paper, we construct a series of simulation models with these two types of defects, which are distributed randomly in CHCs. After constructing CHCs containing different defect types, MD simulations are carried out to calculate the mechanical and thermal properties of defective CHCs with different defect concentrations. Here, the defect concentration is defined as the ratio of the number of rotated or removed sidewalls in a defective CHC to the total number of sidewalls in the corresponding defect-free CHC. In calculations, three CHC samples are considered for each defect concentration and their mean value is taken as the final result.

2.2. MD simulations on the mechanical and thermal properties of CHCs

In the present study, all MD calculations were performed by using large-scale atomic/molecular massively parallel simulator (LAMMPS) MD package [35]. The periodic boundary conditions were applied in all directions, which can effectively avoid the boundary effect and thus
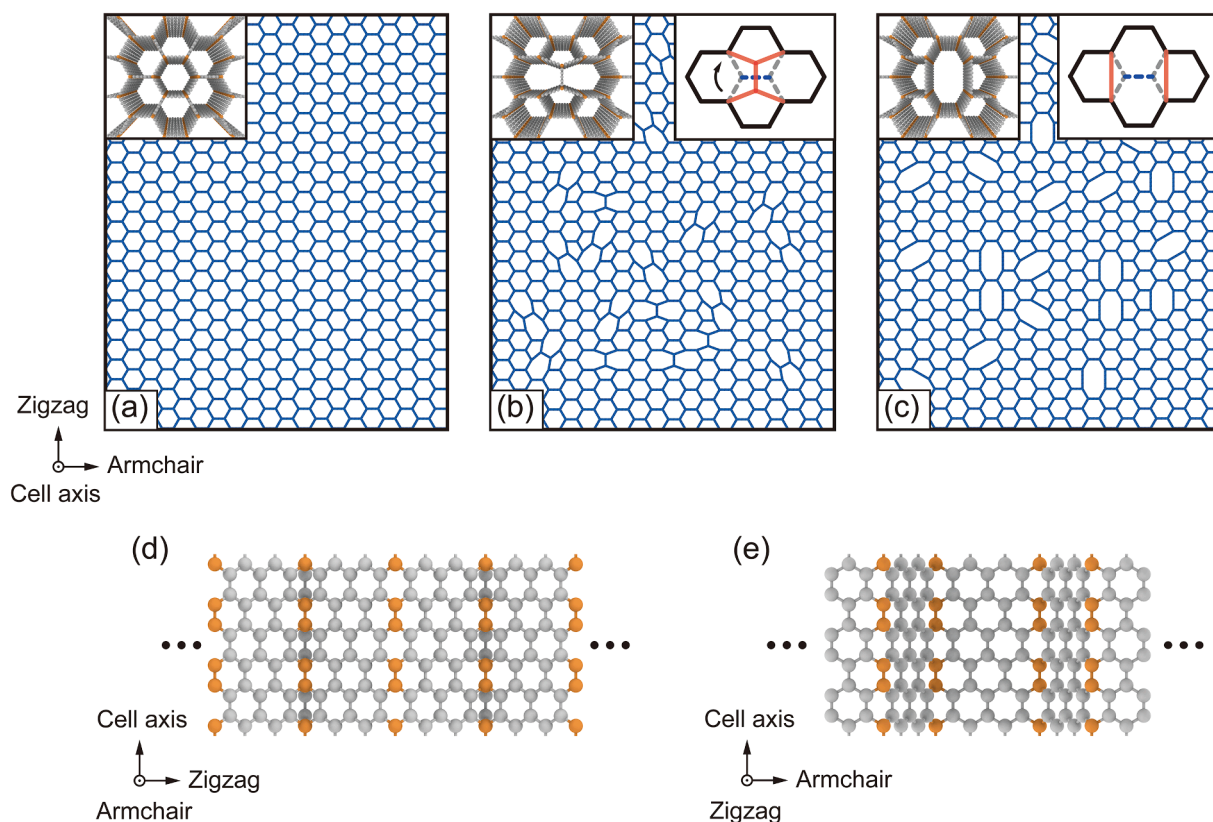
Fig. 2. Top-view of structures of (a) the defect-free CHC, (b) the CHC containing randomly distributed SW defects, and (c) the CHC containing randomly distributed SV defects. The left perspective insets in (a–c) show the detailed structure of perfect CHC, SW and SV defects. The right insets in (b) and (c) are schematics of the formation of SW and SV defects. (d) Side-view and (e) front-view of the defect-free CHC.
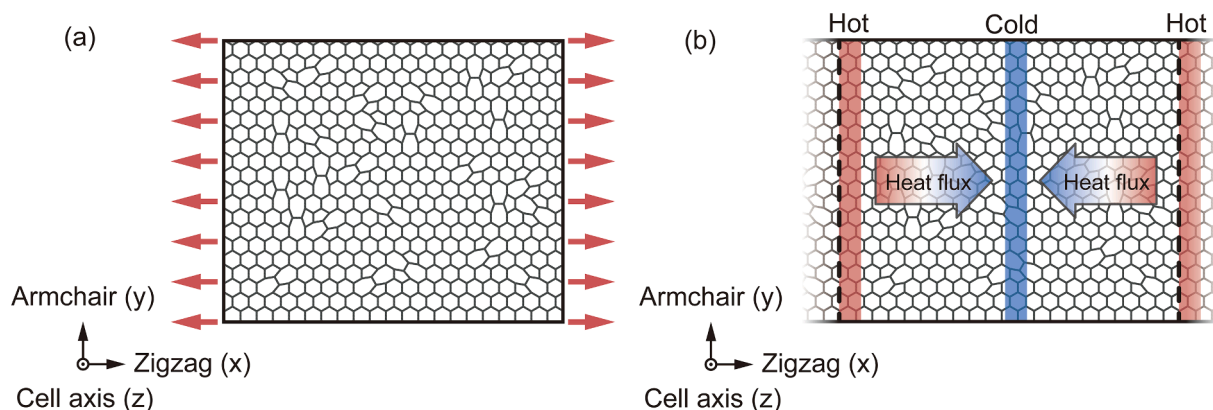

Fig. 3. MD simulation set-ups for (a) the uniaxial tensile test and (b) the thermal conductivity calculation.

equivalently simulate the relatively large CHC structures synthesized in experiments. Actually, similar periodic boundary conditions were widely employed in previous MD simulations on the mechanical and thermal behaviors of various 3D carbon nanomaterials, such as CHCs [25,27,30,32] and graphene-based carbon foams [36–38]. Here, the optimized Tersoff potential developed by Lindsay and Broido [39] was used to simulate the C–C interaction in the component GNRs of CHCs. This potential has been successfully used in previous studies to predict thermal and mechanical responses of carbon-based materials, such as graphene [39–41], CNTs [39,42], graphene foams [43], etc. It should be noted that all simulations were based on the structures constructed by the method as introduced in Section 2.1. In all MD simulations, the time step was set as 1 fs. To validate the reliability of the time step selected here, we calculated the total energy of defect-free CHCs in

microcanonical (NVE) ensemble. As shown in Fig. S1, the total energy is almost unchanged in the NVE ensemble for 100 ps, which proves that the time step of 1 fs is appropriate for our simulations.

To study the mechanical properties of defect-free and defective CHCs, the uniaxial tensile test illustrated in Fig. 3a was employed at the room temperature (300 K). In doing this, an energy minimization was firstly performed using the conjugate gradient algorithm. The system was then relaxed within the isothermal-isobaric (NPT) ensemble at the temperature of 300 K and zero external pressure for 20 ps. As shown in Fig. S2, values of the total energy, length and temperature of defect-free CHCs all keep unchanged after ~ 20 ps, which indicates that the system has reached the equilibrium state. Afterwards, the uniaxial tensile test was performed by expanding the box size in the × direction with a strain rate of 10^9 s^{-1} in the NPT ensemble. The strain rate chosen here can
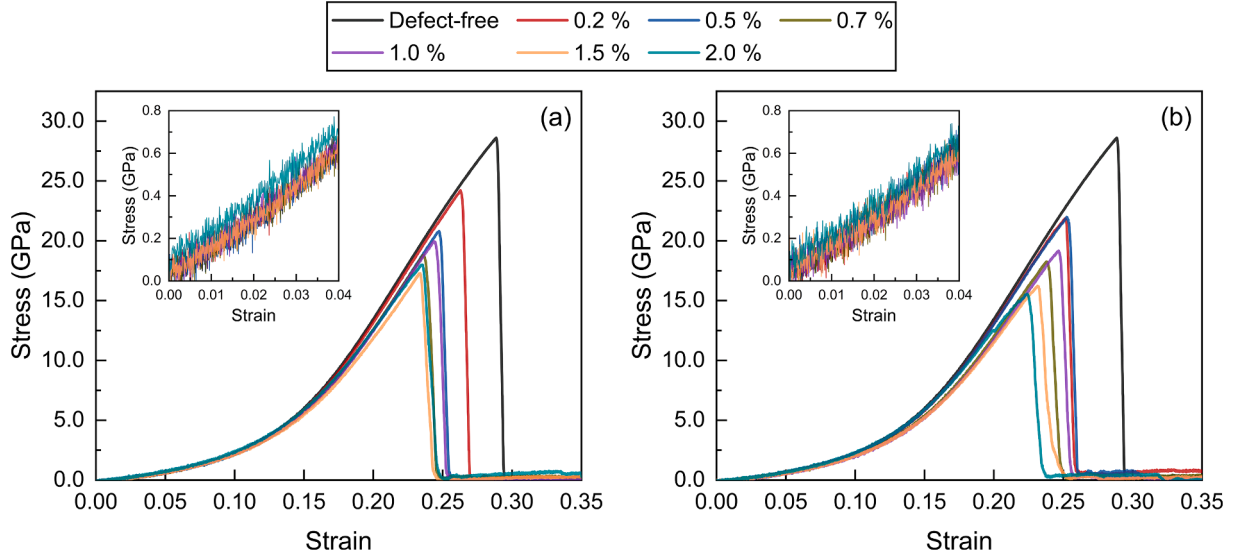
Fig. 4. Stress-strain curves of CHCs with different concentrations of (a) SW defects and (b) SV defects. The insets show the regions used to calculate the Young's modulus of CHCs.

equivalently simulate the quasi-static load applied to CHCs and, meanwhile, can retain the efficiency of MD simulations, since, as shown in Fig. S3, no significant changes are observed in the mechanical properties if we keep decreasing the strain rate from 10^9 s^{-1}. Actually, the same strain rate of 10^9 s^{-1} was also widely employed in previous MD simulations on mechanical behaviors of the defect-free CHCs [24–26,28,29].

Here, in order to provide an accurate uniaxial stress condition at the room temperature, the temperature and pressure damping parameters (along the y and z direction) were set as 10 fs and 1 ps, respectively. Meanwhile, the data of stress and strain was output every 0.1 ps. Finally, the Young's modulus E of CHCs was obtained by calculating the slope of linear part of stress-strain curves. The tensile strength and fracture strain were extracted from these stress-strain curves directly.

In this study, the thermal conductivity of CHCs was evaluated by using the NEMD method. As shown in Fig. 3b, we divided the simulation box into 20 slabs along the × direction. Here, a heat source region and a heat sink region were adjacent to the first and the 11th slabs, respectively. The initial configuration of CHCs was relaxed to its energy-minimized configuration by using the conjugate gradient method firstly. The system was then relaxed at the room temperature (300 K) using constant temperature simulations by the Nosé-Hoover thermostat method (NVT) for 20 ps. As shown in Fig. S4, the total energy, pressure and temperature of CHCs are almost unchanged after ∼ 20 ps, indicating that the structures have reached their equilibrium states. Finally, by using the Langevin thermostat in the NVE ensemble, the temperatures of the heat source and heat sink were set as 330 K and 270 K, respectively. During NEMD simulations, a heat flux (J) can be generated due to the energy exchanges between the hot and cold reservoirs, which results in a temperature gradient (dT/dx) along the × direction. The heat flux along the x-direction (J) can be calculated by [44]:

$$J = \frac{dE_a/dt}{A_c},$$ (1)

where E_a is the accumulated energy, t is the simulation time and A_c is the cross-sectional area of CHCs.

In this work, the temperature T_i of the ith slab was computed by [45]:

$$T_i = \frac{2}{3N_i K_B}\sum_j \frac{p_j^2}{2m},$$ (2)

where N_i is the number of atoms in the ith slab, K_B is the Boltzmann constant, p_j is the momentum of atom j, and m is the atomic mass of

carbon atom. When the temperature gradient along the heat flux direction reaches the linear state, the thermal conductivity of CHCs (κ) can be calculated by using the Fourier law [44]:

$$\kappa = \frac{J}{dT/dx}.$$ (3)

It is noted that NEMD simulations in NVE ensemble were continued for another 200 ps after the temperature gradient has become stable. The temperature gradient along the heat flux direction was thus obtained by averaging over the 200 ps MD simulations. The LAMMPS code for calculating the thermal conductivity of CHCs is shown in Supplementary materials.

3. Results and discussion

3.1. Validation of models

In order to verify the accuracy of the MD simulation models and the optimized Tersoff potential in dealing with the mechanical and thermal responses of CHCs, the mechanical and thermal properties of SLG were studied, since it can be treated as the basic component of CHCs. The length (along the loading or the heat flux direction) of SLG is 50.18 nm, while the width is 10.22 nm. Meanwhile, the thickness of SLG is assumed to be 3.4 Å [46]. In general, the simulation methods employed here are the same as those introduced in Section 2.2. More details are provided in the Supplementary material. As shown in Tab. S1, the Young's modulus of SLG extracted from our MD simulations is around 923 GPa. Meanwhile, Fig. S5 shows that the tensile strength and the fracture strain of SLG estimated from the present MD simulations are 136.16 GPa and 0.24, respectively. These values are in accordance with the experimental results [10] 1000 ± 100 GPa (Young's modulus), 130 ± 10 GPa (tensile strength), and 0.25 (fracture strain). Moreover, a thermal conductivity around 408.5 W/mK is obtained for the SLG in the present study, which is in good agreement with the value 400 W/mK predicted in the previous studies [47] on the SLG with the same length. The good agreement between the present and previous studies suggests the accuracy of the proposed MD simulation methods and the optimized Tersoff potential in evaluating the mechanical and thermal properties of graphene-based materials such as the CHCs considered here.
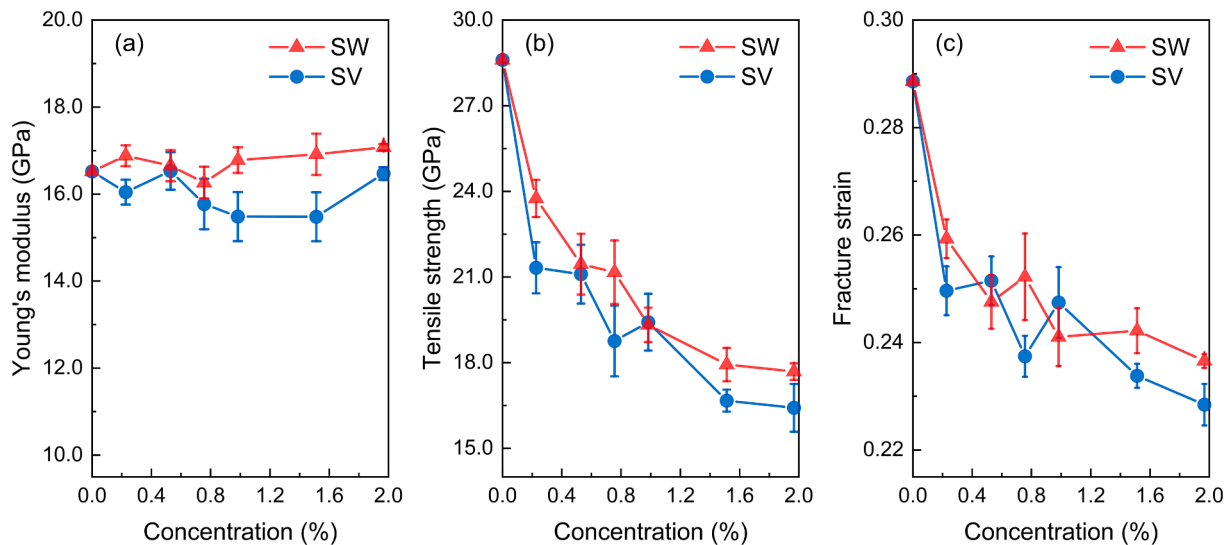
Fig. 5. (a) Young's modulus, (b) tensile strength, and (c) fracture strain of CHCs with different concentrations of SW defects and SV defects.

3.2. Mechanical properties

Based on the MD simulation technique introduced above, we firstly examined the mechanical behaviors of CHCs with three different sizes: $14.58 \times 11.07 \times 1.28$ nm^3, $26.84 \times 22.14 \times 1.28$ nm^3, and $39.62 \times 33.21 \times 1.28$ nm^3, which contain 11220, 42,840 and 94,860 atoms, respectively. As shown in Fig. S7, the stress-strain curves of three defect-free CHCs with different sizes are almost identical to each other, indicating that geometric size also has no influence on the mechanical properties of CHCs. This because the boundary effects are excluded from the present simulation models, since the periodic boundary conditions are employed in the present study. Based on this finding, unless otherwise stated, CHCs having the dimension of $26.84 \times 22.14 \times 1.28$ nm^3 are considered in the following discussion.

The uniaxial tensile tests are subsequently performed to CHCs with SW and SV defects. The defect concentration of defective CHCs ranges from 0.2% to 2.0%. For the sake of comparison, the same MD-based uniaxial tensile test was also performed to defect-free CHCs. The stress-strain curves obtained in the uniaxial tensile tests of CHCs are shown in Fig. 4. It is found that after a short linear region at the low strain level, a nonlinear relation is generally found between the stress and strain until the stress and strain reach the threshold values, i.e., the tensile strength and fracture strain. After the fracture strain, the stress in all CHCs suddenly drops to zero, indicating the brittle fracture occurring in defect-free and defective CHCs [48]. A similar brittle fracture of defect-free CHCs was also observed in previous MD studies [25,28,29]. Here, the tensile strength and fracture strain of defect-free CHCs are, respectively, 28.61 GPa and 0.29, which indicate the high strength and the excellent ductility existing in CHCs. It is noted that these values are close to but slightly smaller than the results 30 GPa (tensile strength) and 0.35 (fracture strain) extracted from previous DFT calculations [23]. The slightly smaller values extracted from the present MD simulations can be attributed to the so-called thermal-softening effect, since previous DFT calculations were conducted without considering the temperature effect, while the present MD simulations were performed at the room temperature.

In Fig. 5, we show the Young's modulus, tensile strength and fracture strain of CHCs with different defect concentrations. It is noted that the Young's modulus was calculated from the slope of the stress–strain curves at the initial linear regions, which are shown in the insets of Fig. 4. When the defect concentration of CHCs increases from 0 (perfect CHCs) to 2%, it is found in Fig. 5a that the Young's modulus E of CHCs containing SW and SV defects is almost independent with the defect

concentration. In this process, E of CHCs containing SW and SV defects rises and falls around the mean value 16.74 GPa and 15.98 GPa, respectively. The deviation of this average value of CHCs containing SW defects from the maximum or minimum E is less than 4%. Similarly, the deviation of the averaged E of CHCs containing SV defects from their maximum or minimum values is less than 3%. This slight impact of defect concentration on the Young's modulus of CHCs can be understood by the damage mechanics theory [49]. According to the damage mechanics theory, the Young's modulus of defective CHCs can be approximately written as $E = E_0 (1–D)$. Here, E_0 is the Young's modulus of defect-free CHCs, and D is the so-called damage factor, which, in the present study, equals to the defect concentration. Since a defect concentration smaller than 2% is considered in the present study, according to the above equation, the Young's modulus E of defective CHCs is almost independent with the defect concentration. In contrast to the Young's modulus, both the tensile strength and the fracture strain of CHCs are found to strongly rely on the defect concentration. Generally, as shown in Fig. 5b and c the tensile strength and the fracture strain decrease as the defect concentration increases. For instance, when the defect concentration increases from 0 to 2%, the tensile strength and fracture strain of CHCs containing SW defects, respectively, decrease from 28.61 GPa and 0.29 to 17.69 GPa and 0.24. In the same process, the tensile strength and fracture strain of CHCs containing SV defects decrease from 28.61 GPa and 0.29 to 16.42 GPa and 0.23, respectively. The significant influence of cell defects on the fracture properties of CHCs can be well understood by the classical fracture mechanics theory. If the defect-free CHC is treated as a pristine material, the heptagonal or octagonal cells in the defective CHC can be modelled as cracks. This is a reasonable continuum level analog of heptagonal or octagonal cells, since these cells are larger than hexagonal cells and thus can be treated as cracks or voids in the material. The stress concentration can occur in the region near these "cracks", which becomes more significant as the crack number increases. As a result, the tensile strength and fracture strain of CHCs can be reduced due to the existence of defects. The reduction in the tensile strength and fracture strain become more significant as the defect concentration grows. Moreover, from Fig. 5b and c we also see that the impact of SV defects on the tensile strength and fracture strain of CHCs is generally larger than that of their SW counterparts. The more significant influence of SV defects can be understood by the fact that the crack size (octagonal cell) of CHCs containing SV defects is larger than that (heptagonal cell) of their counterparts containing SW defects. It is noted that at the defect concentrations of 0.5% and 1%, there exist an exception that the tensile strength and fracture
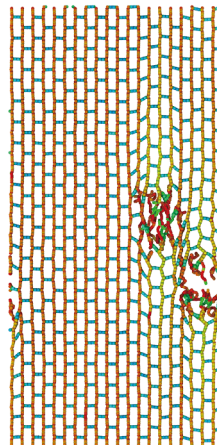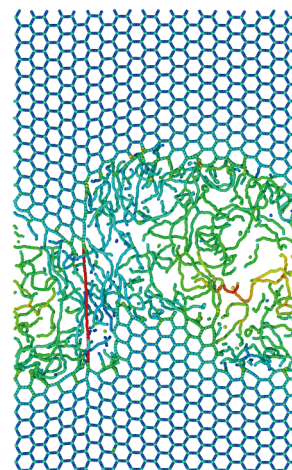
Defect-free CHC
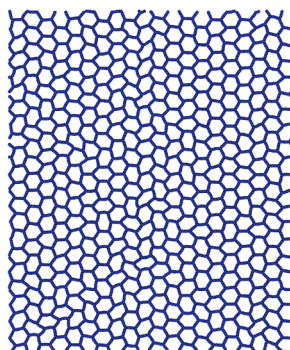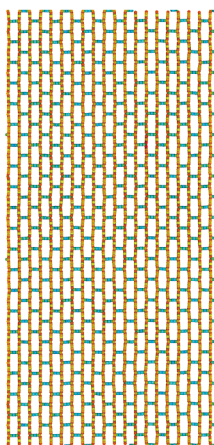
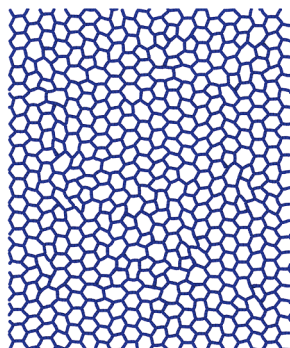(a) Equilibrated, strain=0.0   (b) strain=0.287   (c) strain=0.2905   (d) strain=0.35
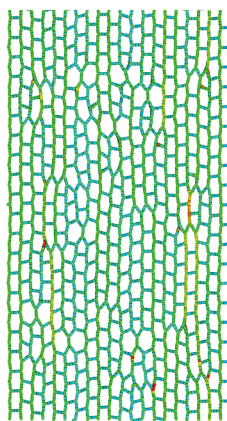
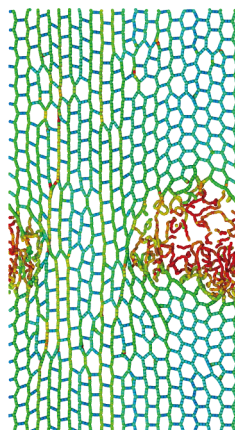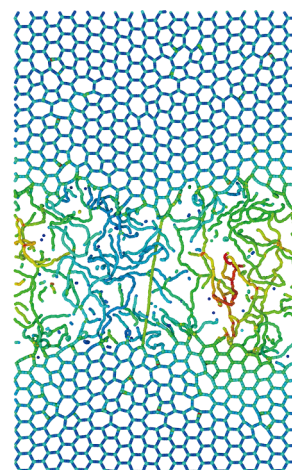**2% SW CHC**

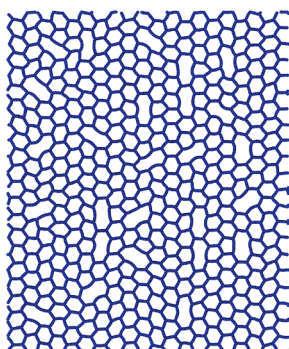(e) Equilibrated, strain=0.0   (f) strain=0.21   (g) strain=0.238   (h) strain=0.35
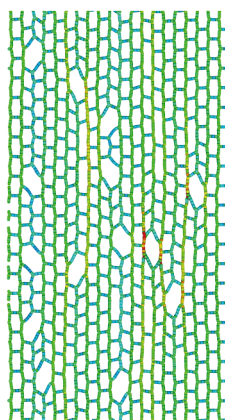
2% SV CHC

(i) Equilibrated, strain=0.0   (j) strain=0.21   (k) strain=0.2275   (l) strain=0.35
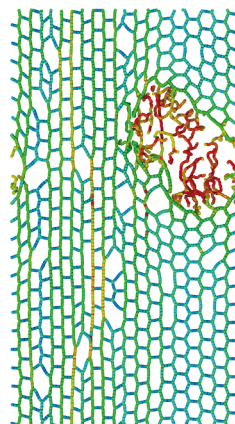
von Mises Stress (GPa)
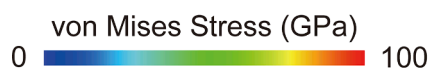
0 [color bar] 100
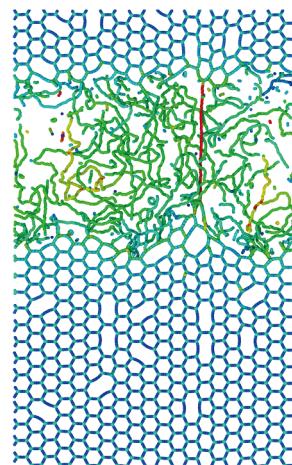
Fig. 6. The deformation processes and von Mises stress evolution of CHCs at various strain levels. (a–d) Defect-free CHC, (e–h) CHC with 2% SW defects, and (i–l) CHC with 2% SV defects.
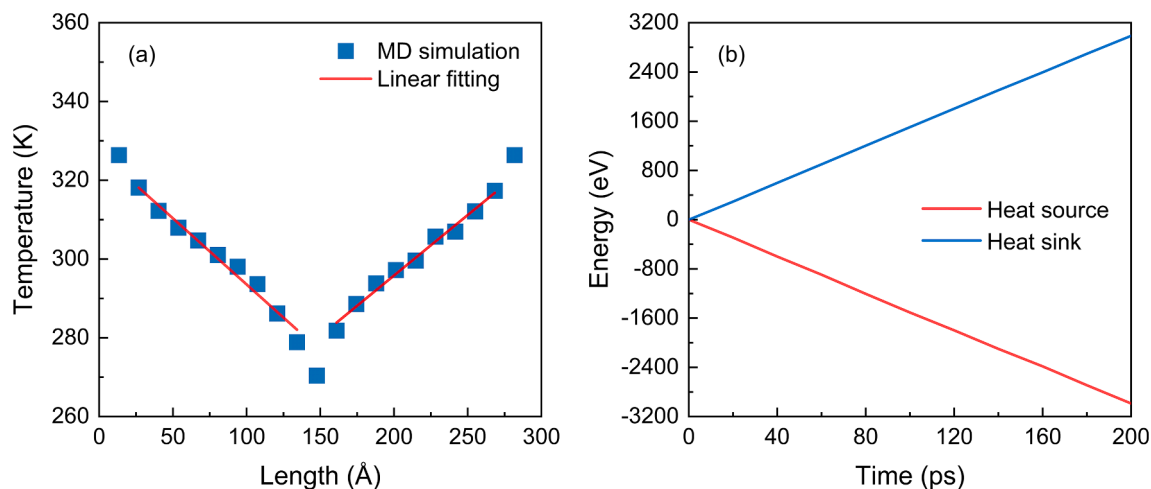
Fig. 7. (a) Linear-state temperature distribution of defect-free CHCs obtained in NEMD simulations at 300 K. (b) Energies added to the heat source and removed from the heat sink during the simulation.
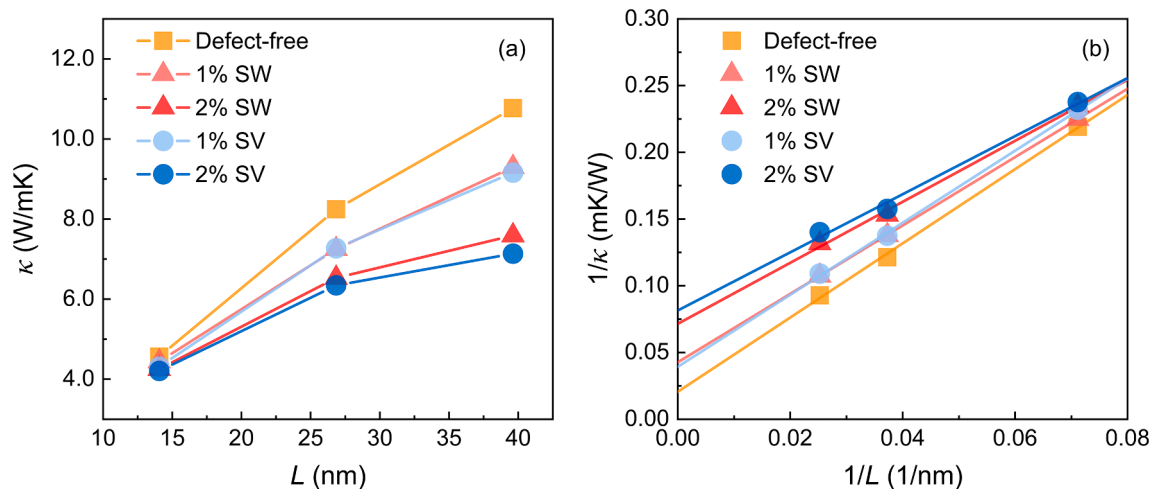

Fig. 8. (a) The thermal conductivity of defect-free and defective CHCs with different lengths. (b) Relation between the inverse thermal conductivity and the inverse length of CHCs.

strain of CHCs containing SW defects are larger than those of CHCs containing SV defects. This exception can be partly attributed to the randomness of defect orientation as shown in Fig. 2.

The deformation process and von Mises stress evolution of defect-free and defective CHCs during the uniaxial tensile test are shown in Fig. 6. As for the defect-free CHCs shown in Fig. 6a and 6b, the shape of CHC cells initially transforms from hexagon into rectangle. The largest stress is observed in cell walls parallel to the loading direction, whose magnitude is about two times larger than that of the stress in other cell walls. Therefore, as observed in Fig. 6c, the initial fracture occurs in these cell walls parallel to the loading direction. The ruptured cells generate plenty of single carbon chains at the strain of 0.35 (Fig. 6d). A similar phenomenon is also observed in previous MD simulations of CHCs [28,29] based on the AIREBO potential [50]. In the CHCs with SW defects, the stress concentration is observed in their defective cells. Moreover, compared to the defect-free CHCs, a more significant stress concentration is observed in the present CHCs containing SW defects (Fig. 6f), as the ratio of the maximum stress and the minimum stress (or the factor of stress concentration) now is about 5.5. Due to the effect of stress concentration, the initial fracture occurs at the SW defects rather than at cells parallel to the loading direction (Fig. 6g). The initial fracture leads to the breaking of a number of cell walls and thus induces the formation of more single carbon chains (Fig. 6h) before the final rupture.

As shown in Fig. 6i–l, the structure evolution of CHCs containing SV defects is similar to that of their counterparts containing SW defects. Specifically, the initial fracture occurs at the places where SV defects exist. Meanwhile, according to Fig. 6j, the factor of stress concentration of CHCs with SV defects is about 6.3, which is much larger than the value of CHCs with SW defects. As a result, smaller tensile strength and fracture strain are expected in CHCs with SV defects, which is indeed consistent with the MD results shown in Fig. 5.

3.3. Thermal properties

By using the technique detailed in Section 2.2, we investigate the influence of SW and SV defects on the thermal conductivity of CHCs in this subsection. As an example, in Fig. 7a we show the temperature distribution in a defect-free CHC. We find a linear temperature gradient between the hot and cold slabs in NEMD simulations. Meanwhile, as shown in Fig. 7b, we find that the magnitude of the energy flux passing the hot and cold slabs are close to each other. Therefore, the total energy is accurately conserved.

In Fig. 8a, we show the thermal conductivity of CHCs with different lengths in the heat flux direction, ranging from 14.58 to 39.62 nm. Here, defect-free CHCs and defective CHCs containing SW and SV defects are both considered. It is found that the thermal conductivity of both defect-
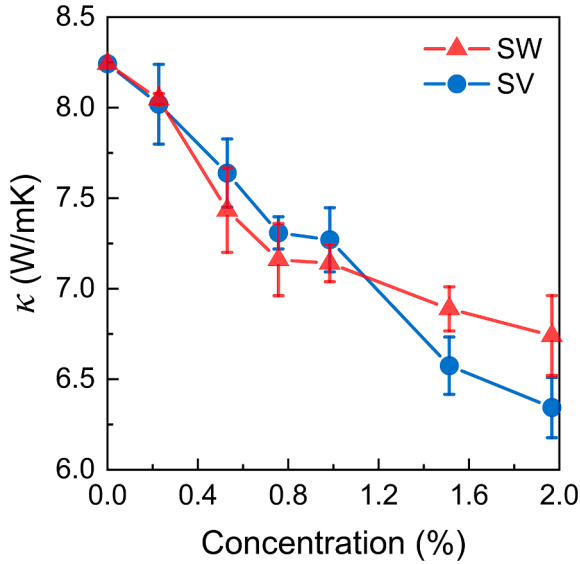
Fig. 9. Thermal conductivity of CHCs with different concentrations of SW defects and SV defects.

Fig. 10. The calculated PDOS of defect-free CHCs and defective CHCs containing 2% SW and SV defects.

free and defective CHCs increases as their length L grows. The similar length dependence of the thermal conductivity was also observed in recent NEMD simulations on CHCs [30,32]. It is revealed in the previous study [51] that when the sample size is smaller than the phonon mean free path, the additional interface scattering is dominant in the heat transport. However, when the sample size approaches dramatically large, the interface scattering will disappear, which thus will result in the disappearance of length dependence of the thermal conductivity. According to the kinetic theory, the relation between the thermal conductivity of CHCs κ and their length in the heat flux direction L can be expressed as [51]:

$$\frac{1}{\kappa} = \frac{1}{\kappa_\infty}\left(\frac{l_p}{L} + 1\right), \tag{4}$$

where κ_∞ is the size-independent thermal conductivity of CHCs with the infinite length, and l_p is the effective phonon mean free path. In Fig. 8b, we show the inverse thermal conductivity ($1/\kappa$) of CHCs against their inverse length ($1/L$). By fitting Eq. (4) to the MD simulation results, we can obtain the size-independent thermal conductivity of defect-free CHCs, which is 47.62 W/mK. This value exactly agrees with ~ 50 W/mK obtained from the previous study [30,32] based on NEMD simulations.

In Fig. 9, we show the thermal conductivity κ of CHCs with various defect concentrations extracted from NEMD simulations. Here, the length in the heat flux direction of CHCs is 26.84 nm. Our results indicate that the thermal conductivity of CHCs decreases significantly as the defect concentration increases. For example, when the defect concentration increases from 0 to 2%, the thermal conductivities of CHCs with SW defects and SV defects are, respectively, reduced by 18% and 23%. To reveal the physical mechanism behind the reduction in the thermal conductivity of defective CHCs, we resort to phonon density of states (PDOS) of atoms in the CHC system. Here, the PDOS can be obtained after conducting the following Fourier transformation of atomic velocities autocorrelation functions at equilibrium state within NVE ensemble [52]:

$$\text{PDOS}(\omega) = \int \frac{\langle \sum_{i=1}^{N} \boldsymbol{v}_i(t) \cdot \boldsymbol{v}_i(0)\rangle}{\langle \sum_{i=1}^{N} \boldsymbol{v}_i(0) \cdot \boldsymbol{v}_i(0)\rangle} \cdot \exp(-2\pi i\omega t)\mathrm{d}t, \tag{5}$$

where N is the total number of atoms, ω is the phonon frequency, $\boldsymbol{v}_i(t)$ and $\boldsymbol{v}_i(0)$ are the velocities of the ith carbon atoms at the moment t and initial time, respectively, and $\langle \cdots \rangle$ means the atom number-averaged
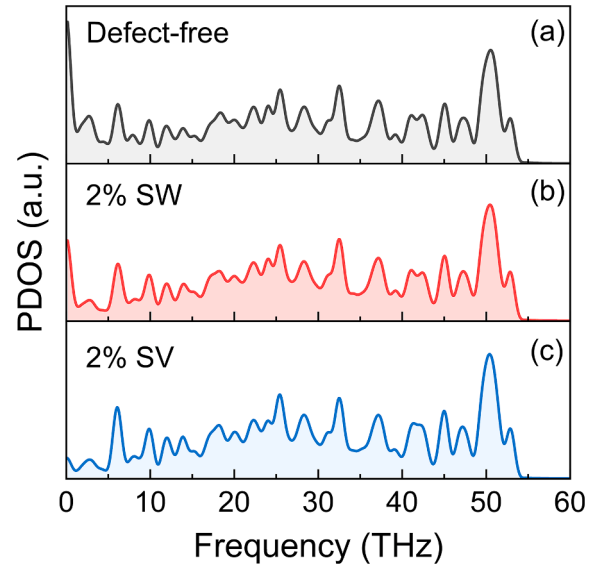
velocity autocorrelation function.

Taking the CHC with 2% SW and SV defects as an example, in Fig. 10 we show PDOS of defective CHCs. For the sake of comparison, the result of defect-free CHC is also presented in this figure. We find that the high frequency peaks of defect-free CHCs and defective CHCs have the similar value around 50 THz. However, the PDOS of defective CHCs is suppressed at the low-frequency (0–5 THz), which indicates more phonon scattering existing in defective CHCs. As a result, a defective CHC is expected to possess a smaller phonon mean free path and thus have a lower thermal conductivity. These observations are in good agreement with previous studies indicating that the thermal conductivity is dominated by low-frequency phonons [53]. Moreover, the PDOS of CHCs with SV defects is lower than that of CHCs with SW defects, which indicates that the thermal conductivity of the former is smaller than that of the latter. This prediction is consistent with NEMD results shown in Fig. 9. Based on the above results, we can come to the conclusion that both SW and SV defects can significantly reduce the thermal conductivity of CHCs, which can be partly attributed to more phonon scattering in CHCs with a higher defect concentration.

In this work, more phonon scattering observed in defective CHCs originates from the wavy configuration of the component GNRs in defective CHCs. In Fig. 11, we show the energy minimized structures of defect-free CHCs and those of their counterparts containing defects. It is observed that the existence of SW and SV defects results in the significant cell wall curvature in CHCs. By contrast, the components GNRs in defect-free CHCs can keep the flat configuration after the energy minimization. Previous MD simulation studies [32,47] indicate that the curvature of GNRs plays a critical role in reducing the thermal conductivity of graphene-based materials. Therefore, more phonon scattering and lower thermal conductivity are expected in the CHCs with a higher defect concentration, since a higher defect concentration can lead to a larger degree of cell wall curvature.

From Fig. 9 we can also see that at a relatively large defect concentration, e.g., 2%, the reduction in the thermal conductivity of CHCs with SV defects is more significant than that of CHCs with SW defects. In addition to more phonon scattering existing in CHCs with SV defects mentioned above, the more significant reduction in the thermal conductivity of CHCs with SV defects is also attributed to their smaller density. According to the phonon kinetic theory [54], the lattice thermal conductivity of a material is determined by $\kappa \sim Cvl_p$, where C is the heat capacity and v is the phonon group velocity. Different to the SW defect that is generated by rotating the cell wall, the SV defect is generated by
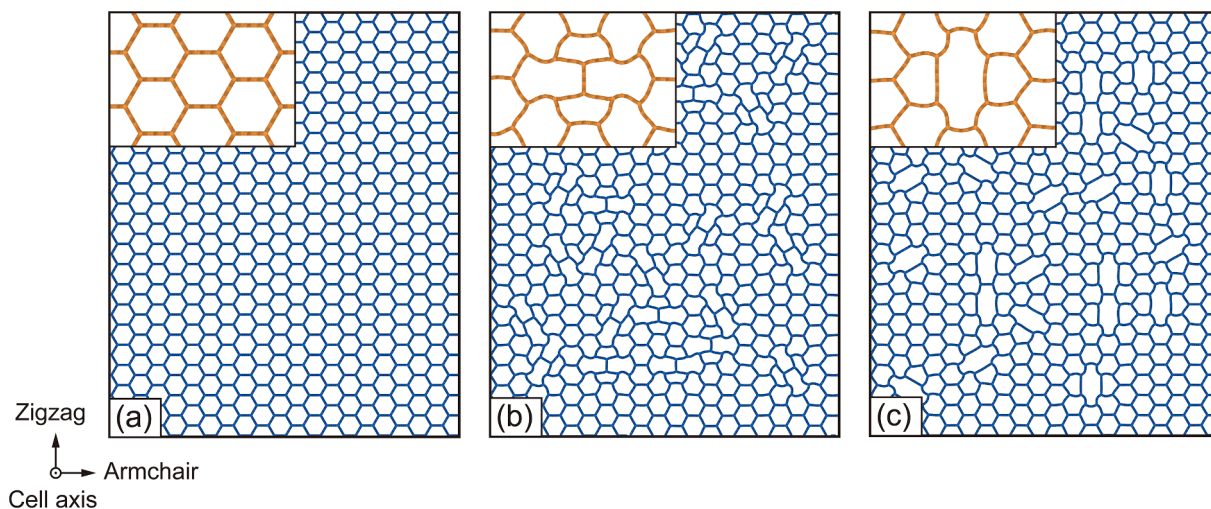
Fig. 11. The energy minimized structures of (a) the defect-free CHC, (b) the CHC with SW defects, and (c) the CHC with SV defects. The insets show the local configuration of cells in CHCs.

removing one cell wall. Thus, the density of CHCs with SV defects should be smaller than that of their counterparts with SW defects. This difference will become larger as the defect concentration increases. It is known that a material with a smaller density is theoretically expected to have a smaller heat capacity and thus a lower thermal conductivity. Therefore, the smaller density of CHCs with SV defects can be another important factor that is responsible for the lower thermal conductivity observed in them, especially when the defect concentration is relatively large.

4. Conclusions

In this work, by using MD simulations, we provide a comprehensive assessment of the influence of cell defects on the mechanical and thermal properties of CHCs. Two defect types, i.e., SW and SV defects, which distribute randomly in CHCs are considered in our study. Our results show that the Young's modulus of defective CHCs is almost independent with the defect concentration. However, both the tensile strength and the fracture strain can be greatly reduced by the cell defects, which becomes more significant as the defect concentration increases. Moreover, when compared to the SW defects, the effect of SV defect on the fracture properties of CHCs is much larger. The effect of cell defects on the Young's modulus and fracture properties is well explained by the theories of damage and fracture mechanics.

As for the thermal property, our results show that both SW and SV defects can reduce the thermal conductivity of CHCs. Specifically, the reduction in thermal conductivity increases as the defect concentration increases. The wavy configuration of the component graphene elements in defective cells of CHCs accounts for this reduction in thermal conductivity, since, according to our PDOS analysis, it can increase the phonon scattering of CHCs and thus reduce the thermal conductivity. Moreover, the effect of SV defects on the thermal conductivity of CHCs is found to be larger than that of SW effects when the defect concentration is relatively large. The more significant effect of SV defects on the thermal conductivity of CHCs can be attributed to the fact that, the heat capacity of CHCs with SV defects is smaller than that of their counterparts with SW defects.

Overall, our study provides a more precise understanding of the mechanical and thermal property of CHCs, which is helpful for the property prediction and engineering applications of CHCs in the future.

5. Data availability

The raw/processed data required to reproduce these findings are available from the corresponding author on reasonable request.

CRediT authorship contribution statement

Yao Du: Conceptualization, Methodology, Software, Investigation, Validation, Formal analysis, Writing - original draft, Writing - review & editing. **Jianli Zhou:** Data curation, Formal analysis. **Penghua Ying:** Data curation, Formal analysis. **Jin Zhang:** Conceptualization, Formal analysis, Resources, Writing - review & editing, Supervision, Project administration, Funding acquisition.

Declaration of Competing Interest

We declare that we have no financial and personal relationships with other people or organizations that can inappropriately our work. There is no professional or other personal interest of any nature or kind in any product, service or company that could be constructed as influencing the position presented in, or the review of, the manuscript entitled.

Acknowledgments

Appendix A. Supplementary data

Supplementary data to this article can be found online at https://doi.org/10.1016/j.commatsci.2020.110125.

References

[1] H.W. Kroto, J.R. Heath, S.C. O'Brien, R.F. Curl, R.E. Smalley, C60: Buckminsterfullerene, Nature 318 (1985) 162–163, https://doi.org/10.1038/318162a0.

[2] J. Coro, M. Suárez, L.S.R. Silva, K.I.B. Eguiluz, G.R. Salazar-Banda, Fullerene applications in fuel cells: A review, Int. J. Hydrogen Energy 41 (2016) 17944–17959, https://doi.org/10.1016/j.ijhydene.2016.08.043.

[3] S. Iijima, Helical microtubules of graphitic carbon, Nature 354 (1991) 56–58, https://doi.org/10.1038/354056a0.

[4] M.M.J. Treacy, T.W. Ebbesen, J.M. Gibson, Exceptionally high Young's modulus observed for individual carbon nanotubes, Nature 381 (1996) 678–680, https://doi.org/10.1038/381678a0.

[5] J.P. Lu, Elastic properties of carbon nanotubes and nanoropes, Phys. Rev. Lett. 79 (1997) 1297–1300, https://doi.org/10.1103/PhysRevLett.79.1297.

[6] S. Berber, Y.-K. Kwon, D. Tománek, Unusually high thermal conductivity of carbon nanotubes, Phys. Rev. Lett. 84 (2000) 4613–4616, https://doi.org/10.1103/PhysRevLett.84.4613.

[7] V. Popov, Carbon nanotubes: Properties and application, Mater. Sci. Eng. 43 (2004) 61–102, https://doi.org/10.1016/j.mser.2003.10.001.

[8] M.F.L. De Volder, S.H. Tawfick, R.H. Baughman, A.J. Hart, Carbon nanotubes: Present and future commercial applications, Science. 339 (2013) 535–539, https://doi.org/10.1126/science.1222453.

[9] K.S. Novoselov, A.K. Geim, S.V. Morozov, D. Jiang, Y. Zhang, S.V. Dubonos, I. V. Grigorieva, A.A. Firsov, Electric field effect in atomically thin carbon films, Science. 306 (2004) 666–669, https://doi.org/10.1126/science.1102896.

[10] C. Lee, X. Wei, J.W. Kysar, J. Hone, Measurement of the elastic properties and intrinsic strength of monolayer graphene, Science 321 (2008) 385–388, https://doi.org/10.1126/science.1157996.

[11] A.A. Balandin, S. Ghosh, W. Bao, I. Calizo, D. Teweldebrhan, F. Miao, C.N. Lau, Superior thermal conductivity of single-layer graphene, Nano Lett. 8 (2008) 902–907, https://doi.org/10.1021/nl0731872.

[12] S. Bae, H. Kim, Y. Lee, X. Xu, J.-S. Park, Y. Zheng, J. Balakrishnan, T. Lei, H. Ri Kim, Y.I. Song, Y.-J. Kim, K.S. Kim, B. Özyilmaz, J.-H. Ahn, B.H. Hong, S. Iijima, Roll-to-roll production of 30-inch graphene films for transparent electrodes, Nature Nanotech. 5 (2010) 574–578, https://doi.org/10.1038/nnano.2010.132.

[13] F. Xia, T. Mueller, Y. Lin, A. Valdes-Garcia, P. Avouris, Ultrafast graphene photodetector, Nature Nanotech. 4 (2009) 839–843, https://doi.org/10.1038/nnano.2009.292.

[14] R.J. Young, I.A. Kinloch, L. Gong, K.S. Novoselov, The mechanics of graphene nanocomposites: A review, Compos. Sci. Technol. 72 (2012) 1459–1476, https://doi.org/10.1016/j.compscitech.2012.05.005.

[15] D.A. Dikin, S. Stankovich, E.J. Zimney, R.D. Piner, G.H.B. Dommett, G. Evmenenko, S.T. Nguyen, R.S. Ruoff, Preparation and characterization of graphene oxide paper, Nature 448 (2007) 457–460, https://doi.org/10.1038/nature06016.

[16] S. Guo, Q. Yang, X. He, K. Liew, Design of 3D carbon nanotube-based nanostructures and prediction of their extra-strong mechanical properties under tension and compression, Comp. Mater. Sci. 85 (2014) 324–331, https://doi.org/10.1016/j.commatsci.2014.01.013.

[17] A.M. Marconnet, M.A. Panzer, K.E. Goodson, Thermal conduction phenomena in carbon nanotubes and related nanostructured materials, Rev. Mod. Phys. 85 (2013) 1295–1326, https://doi.org/10.1103/RevModPhys.85.1295.

[18] R. Saito, G. Dresselhaus, M.S. Dresselhaus, Physical properties of carbon nanotubes, World Scientific: New York (1998), https://doi.org/10.1142/p080.

[19] N.V. Krainyukova, E.N. Zubarev, Carbon honeycomb high capacity storage for gaseous and liquid species, Phys. Rev. Lett. 116 (2016), 055501, https://doi.org/10.1103/PhysRevLett.116.055501.

[20] N.V. Krainyukova, B. Kuchta, L. Firlej, P. Pfeifer, Absorption of atomic and molecular species in carbon cellular structures (Review article), Low Temp. Phys. 46 (2020) 219–231, https://doi.org/10.1063/10.0000705.

[21] Z. Zhang, A. Kutana, Y. Yang, N.V. Krainyukova, E.S. Penev, B.I. Yakobson, Nanomechanics of carbon honeycomb cellular structures, Carbon 113 (2017) 26–32, https://doi.org/10.1016/j.carbon.2016.11.020.

[22] Z. Pang, X. Gu, Y. Wei, R. Yang, M.S. Dresselhaus, Bottom-up design of three-dimensional carbon-honeycomb with superb specific strength and high thermal conductivity, Nano Lett. 17 (2017) 179–185, https://doi.org/10.1021/acs.nanolett.6b03711.

[23] X. Gu, Z. Pang, Y. Wei, R. Yang, On the influence of junction structures on the mechanical and thermal properties of carbon honeycombs, Carbon 119 (2017) 278–286, https://doi.org/10.1016/j.carbon.2017.04.054.

[24] J. Zhang, A nonlocal continuum model for the buckling of carbon honeycombs, Meccanica 53 (2018) 2999–3013, https://doi.org/10.1007/s11012-018-0854-y.

[25] Y. Liu, J. Liu, S. Yue, J. Zhao, B. Ouyang, Y. Jing, Atomistic simulations on the tensile deformation behaviors of three-dimensional graphene, Phys. Status Solidi B. 255 (2018) 1700680, https://doi.org/10.1002/pssb.201700680.

[26] J. Zhang, C. Wang, Buckling of carbon honeycombs: A new mechanism for molecular mass transportation, J. Phys. Chem. C 121 (2017) 8196–8203, https://doi.org/10.1021/acs.jpcc.7b00716.

[27] F. Meng, C. Chen, H. Dianyin, J. Song, Deformation behaviors of three-dimensional graphene honeycombs under out-of-plane compression: Atomistic simulations and predictive modeling, J. Mech. Phys. Solids. 109 (2017) 241–251, https://doi.org/10.1016/j.jmps.2017.09.003.

[28] L. Xie, H. An, C. He, Q. Qin, Q. Peng, Mechanical properties of vacancy tuned carbon honeycomb, Nanomaterials 9 (2019) 156, https://doi.org/10.3390/nano9020156.

[29] Q. Qin, H. An, C. He, L. Xie, Q. Peng, Anisotropic and temperature dependent mechanical properties of carbon honeycomb, Nanotechnology 30 (2019), 325704, https://doi.org/10.1088/1361-6528/ab14a1.

[30] Z. Wei, F. Yang, K. Bi, J. Yang, Y. Chen, Thermal transport properties of all-sp2 three-dimensional graphene: Anisotropy, size and pressure effects, Carbon 113 (2017) 212–218, https://doi.org/10.1016/j.carbon.2016.11.055.

[31] H. Zhang, S. Hu, S. Wang, Y. Chen, H. Wang, Y. Ni, Thermal transport in three-dimensional carbon honeycombs, Chinese J. Phys. 59 (2019) 567–571, https://doi.org/10.1016/j.cjph.2019.04.017.

[32] J. Zhang, Effects of cell irregularity on the thermal conductivity of carbon honeycombs, Carbon. 131 (2018) 127–136, https://doi.org/10.1016/j.carbon.2018.01.097.

[33] N.V. Krainyukova, Y. Bogdanov, B. Kuchta, Absorption-desorption of carbon dioxide in carbon honeycombs at elevated temperatures, Low Temp. Phys. 45 (2019) 325–330, https://doi.org/10.1063/1.5090090.

[34] F. Banhart, J. Kotakoski, A.V. Krasheninnikov, Structural defects in graphene, ACS Nano. 5 (2011) 26–41, https://doi.org/10.1021/nn102598m.

[35] S. Plimpton, Fast parallel algorithms for short-range molecular dynamics, J. Comput. Phys. 117 (1995) 1–19, https://doi.org/10.1006/jcph.1995.1039.

[36] B. Morris, M. Becton, X. Wang, Mechanical abnormality in graphene-based lamellar superstructures, Carbon 137 (2018) 196–206, https://doi.org/10.1016/j.carbon.2018.05.022.

[37] J. Zhang, Q. Xiong, The negative Poisson's ratio in graphene-based carbon foams, Phys. Chem. Chem. Phys. 20 (2018) 4597–4605, https://doi.org/10.1039/C7CP06983A.

[38] F. Liu, R. Zou, N. Hu, H. Ning, C. Yan, Y. Liu, L. Wu, F. Mo, Understanding the mechanical properties and deformation behavior of 3-D graphene-carbon nanotube structures, Mater. Design. 160 (2018) 377–383, https://doi.org/10.1016/j.matdes.2018.09.036.

[39] L. Lindsay, D.A. Broido, Optimized Tersoff and Brenner empirical potential parameters for lattice dynamics and phonon thermal transport in carbon nanotubes and graphene, Phys. Rev. B. 81 (2010), 205441, https://doi.org/10.1103/PhysRevB.81.205441.

[40] B. Mortazavi, S. Ahzi, Thermal conductivity and tensile response of defective graphene: A molecular dynamics study, Carbon 63 (2013) 460–470, https://doi.org/10.1016/j.carbon.2013.07.017.

[41] B. Mortazavi, S. Ahzi, V. Toniazzo, Y. Rémond, Nitrogen doping and vacancy effects on the mechanical properties of graphene: A molecular dynamics study, Phys. Lett. A. 376 (2012) 1146–1153, https://doi.org/10.1016/j.physleta.2011.11.034.

[42] T. Li, Z. Tang, Z. Huang, J. Yu, A comparison between the mechanical and thermal properties of single-walled carbon nanotubes and boron nitride nanotubes, Physica E. 85 (2017) 137–142, https://doi.org/10.1016/j.physe.2016.08.012.

[43] A. Pedrielli, S. Taioli, G. Garberoglio, N.M. Pugno, Mechanical and thermal properties of graphene random nanofoams via Molecular Dynamics simulations, Carbon 132 (2018) 766–775, https://doi.org/10.1016/j.carbon.2018.02.081.

[44] T. Ikeshoji, B. Hafskjold, Non-equilibrium molecular dynamics calculation of heat conduction in liquid and through liquid-gas interface, Mol. Phys. 81 (1994) 251–261, https://doi.org/10.1080/00268979400100171.

[45] F. Müller-Plathe, A simple nonequilibrium molecular dynamics method for calculating the thermal conductivity, J. Chem. Phys. 106 (1997) 6082–6085, https://doi.org/10.1063/1.473271.

[46] J.C. Meyer, A.K. Geim, M.I. Katsnelson, K.S. Novoselov, T.J. Booth, S. Roth, The structure of suspended graphene sheets, Nature 446 (2007) 60–63, https://doi.org/10.1038/nature05545.

[47] B. Mortazavi, A. Rajabpour, S. Ahzi, Y. Rémond, S. Mehdi Vaez Allaei, Nitrogen doping and curvature effects on thermal conductivity of graphene: A non-equilibrium molecular dynamics study, Solid State Commun. 152 (2012) 261–264. https://doi.org/10.1016/j.ssc.2011.11.035.

[48] P. Ying, J. Zhang, Z. Zhong, Mechanical properties of monolayer ternary transitional metal dichalcogenides MoS 2 x Te 2(1–x): A molecular dynamics study, J. Appl. Phys. 126 (2019), 215105, https://doi.org/10.1063/1.5122264.

[49] J. Lemaitre, J.L. Chaboche, Mechanics of solid materials, Cambridge Univ. Press (1990), https://doi.org/10.1017/CBO9781139167970.

[50] S.J. Stuart, A.B. Tutein, J.A. Harrison, A reactive potential for hydrocarbons with intermolecular interactions, J. Chem. Phys. 112 (2000) 6472–6486, https://doi.org/10.1063/1.481208.

[51] P.K. Schelling, S.R. Phillpot, P. Keblinski, Comparison of atomic-level simulation methods for computing thermal conductivity, Phys. Rev. B. 65 (2002), 144306, https://doi.org/10.1103/PhysRevB.65.144306.

[52] J.M. Dickey, A. Paskin, Computer simulation of the lattice dynamics of solids, Phys. Rev. 188 (1969) 1407–1418, https://doi.org/10.1103/PhysRev.188.1407.

[53] A.J.H. McGaughey, E.S. Landry, D.P. Sellan, C.H. Amon, Size-dependent model for thin film and nanowire thermal conductivity, Appl. Phys. Lett. 99 (2011), 131904, https://doi.org/10.1063/1.3644163.

[54] C. Kittel, R.W. Hellwarth, Introduction to solid state physics, 1957. http://physicstoday.scitation.org/doi/10.1063/1.3060399.